Jinst

PUBLISHED BY INSTITUTE OF PHYSICS PUBLISHING AND SISSA

RECEIVED: *April 13, 2007*
ACCEPTED: *May 2, 2007*
PUBLISHED: *May 18, 2007*

Construction, assembly and testing of the ATLAS hadronic end-cap calorimeter

ATLAS Hadronic End-Cap Calorimeter Group

D.M. Gingrich,[a,1] **G. Lachat,**[a] **J. Pinfold,**[a] **J. Soukup,** [a] **D. Axen,**[b] **C. Cojocaru,**[c] **G. Oakham,**[c,1] **M. O'Neill,**[c] **M.G. Vincter,**[c] **M. Aleksa,**[d] **J. Bremer,**[d] **M. Chalifour,**[d,2] **C. Fabre,**[d] **P. Fassnacht,**[d] **A. Gonidec,**[d] **P. Pailler,**[d] **G. Vandoni,**[d] **A. Cheplakov,**[e,3] **V. Datskov,**[e] **V. Drobin,**[e] **A. Fedorov,**[e] **S. Golubykh,**[e] **N. Javadov,**[e,4] **V. Kalinnikov,**[e] **S. Kakurin,**[e] **M. Kazarinov,**[e] **V. Kukhtin,**[e] **E. Ladygin,**[e] **A. Lazarev,**[e] **A. Neganov,**[e] **I. Pisarev,**[e] **N. Rousakovitch,**[e] **E. Serochkin,**[e] **S. Shilov,**[e] **A. Shalyugin,**[e] **Yu. Usov,**[e] **J. Ban,**[f] **D. Bruncko,**[f] **E. Kladiva,**[f] **P. Stavina,**[f,5] **P. Strizenec,**[f] **M. Heldmann,**[g,6] **M. Hohlfeld,**[g,7] **K. Jakobs,**[g,6] **L. Köpke,**[g] **E. Marschalkowski,**[g,8] **D. Meder,**[g,9] **R. Othegraven,**[g] **U. Schäfer,**[g] **D. Schroff,**[g,10] **H. Secker,** [g] **J. Thomas,**[g,11] **W. Walkowiak,**[g,12] **C. Zeitnitz,**[g,9] **G. Azuelos,**[h,1] **P-A. Delsart,**[h] **C. Leroy,**[h] **R. Mazini,**[h,13] **R. Mehdiyev,**[h,4] **A. Akimov,**[i] **M. Blagov,**[i] **A. Komar,**[i] **A. Snesarev,**[i] **M. Speransky,**[i] **V. Sulin,**[i] **M. Yakimenko,**[i,14] **M. Aderholz,**[j] **T. Barillari,**[j] **H. Brettel,**[j] **W. Cwienk,**[j] **J. Fent,**[j] **A. Fischer,**[j] **J. Habring,**[j] **J. Huber,**[j] **A. Karev,**[j,15] **A. Kiryunin,**[j,16] **L. Kurchaninov,**[j,17] **H. Laskus,**[j] **S. Menke,**[j] **P. Mooshofer,**[j] **H. Oberlack,**[j] **D. Salihagic,**[j,18] **P. Schacht,**[j] **H. Schmuecker,**[j] **H. Stenzel,**[j,19] **D. Striegel,**[j] **W. Tribanek,**[j] **J. Zimmer,**[j] **T. Chen,**[k] **J. Ping,**[k] **M. Qi,**[k] **A. Falou,**[l] **G. Macé,**[l] **S. Chekulaev,**[m,1] **S. Denisov,**[m] **M. Levitsky,**[m] **A. Minaenko,**[m] **G. Mitrofanov,**[m] **A. Moiseev,**[m,14] **A. Pleskatch,**[m] **V. Sytnik,**[m,20] **L. Zakamsky,**[m] **P. Benoit,**[n,21] **K.W. Hoyle,**[n,14] **A. Honma,**[n,21] **M.J. Losty,**[n] **R. Maharaj,**[n] **C.J. Oram,**[n*] **E.W. Pattyn,**[n] **M. Rosvick,**[n] **C. Sbarra,**[n,22] **H-P. Wellisch,**[n,21] **M. Wielers,**[n,23] **P.S. Birney,**[o] **M. Dobbs,**[o,24] **M. Fincke-Keeler,**[o] **D. Fortin,**[o] **T.A. Hodges,**[o] **T. Ince,**[o] **N. Kanaya,**[o,25] **R.K. Keeler,**[o] **R. Langstaff,**[o] **M. Lefebvre,**[o] **R.A. McPherson,**[o,26] **D.C. O'Neil,**[o,27] **R. Seuster,**[o] **D. Forbush,**[p] **P. Mockett,**[p] **F. Toevs,**[p] **H.M. Braun**[q]

[a] *University of Alberta, Edmonton, Canada*
[b] *University of British Columbia, Vancouver, Canada*
[c] *Carleton University, Ottawa, Canada*
[d] *European Laboratory for Particle Physics (CERN), Geneva, Switzerland*
[e] *Joint Institute for Nuclear Research, Dubna, Russia*
[f] *Institute of Experimental Physics of the Slovak Academy of Sciences, Kosice, Slovakia*
[g] *Institut für Physik der Universität Mainz, Mainz, Germany*
[h] *Université de Montréal, Montréal, Canada*

2007 JINST 2 P05005

[i]*Lebedev Institute of Physics, Academy of Sciences, Moscow, Russia*
[j]*Max-Planck-Institut für Physik, Munich, Germany*
[k]*University of Nanjing, Nanjing, China*
[l]*Laboratoire de l'Accélérateur Linéaire, Université de Paris-Sud, IN2P3-CNRS, Orsay, France*
[m]*Institute for High Energy Physics, Protvino, Russia*
[n]*TRIUMF, Vancouver, Canada*
[o]*University of Victoria, Victoria, Canada*
[p]*University of Washington, Seattle, U.S.A.*
[q]*University of Wuppertal, Wuppertal, Germany*

[1] *Also TRIUMF, Vancouver, Canada*
[2] *Also CEA Saclay, Gif-sur-Yvette, France*
[3] *Now at University of Glasgow, Glasgow, U.K.*
[4] *On leave of absence from IP, Baku, Azerbaijan*
[5] *Now at Comenius University, Bratislava, Slovakia*
[6] *Now at University of Freiburg, Freiburg, Germany*
[7] *Now at LAL, Orsay, France*
[8] *Now at Dialog Semiconductor GmbH, Munich, Germany*
[9] *Now at University of Wuppertal, Wuppertal, Germany*
[10] *Now at GIP, Mainz, Germany*
[11] *Now at University of Birmingham, Birmingham, U.K.*
[12] *Now at University of Siegen, Siegen, Germany*
[13] *Now at University of Toronto, Toronto, Canada*
[14] *Deceased*
[15] *On leave of absence from JINR, Dubna, Russia*
[16] *On leave of absence from IHEP, Protvino, Russia*
[17] *Now at TRIUMF, Vancouver, Canada*
[18] *On leave of absence from University of Podgorica, Montenegro, Serbia and Montenegro*
[19] *Now at University of Giessen, Giessen, Germany*
[20] *Now at University of California, Riverside, U.S.A.*
[21] *Now at CERN, Geneva, Switzerland*
[22] *Also University of Victoria. Now at Università di Bologna and INFN, Bologna, Italy*
[23] *Also University of Victoria. Now at Rutherford Appleton Laboratory, Chilton, Didcot, U.K.*
[24] *Now at McGill University, Montreal, Canada*
[25] *Now at Kobe University, Kobe, Japan*
[26] *Also Institute of Particle Physics of Canada*
[27] *Now at Simon Fraser University, Burnaby, BC, Canada*

E-mail: Losty@triumf.ca

ABSTRACT: The construction and assembly of the four wheels of the ATLAS hadronic end-cap calorimeter and their insertion into the two end-cap cryostats are described. The results of the qualification tests prior to installation of the two cryostats in the ATLAS experimental cavern are reviewed.

KEYWORDS: Cryogenic detectors, Calorimeters, Large detector systems for particle and astroparticle physics, Detector design and construction technologies and materials.

*Corresponding author

2007 JINST 2 P05005

Contents

2007 JINST 2 P05005

1. Introduction

The hadronic end-cap calorimeter (HEC) of the ATLAS experiment [1] at the CERN Large Hadron Collider (LHC) is a copper-liquid argon sampling calorimeter in a flat plate design. The calorimeter provides coverage for hadronic showers in the pseudorapidity[1] range $1.5 < |\eta| < 3.2$. The HEC shares each of the two liquid argon end-cap cryostats [2] with the electromagnetic end-cap

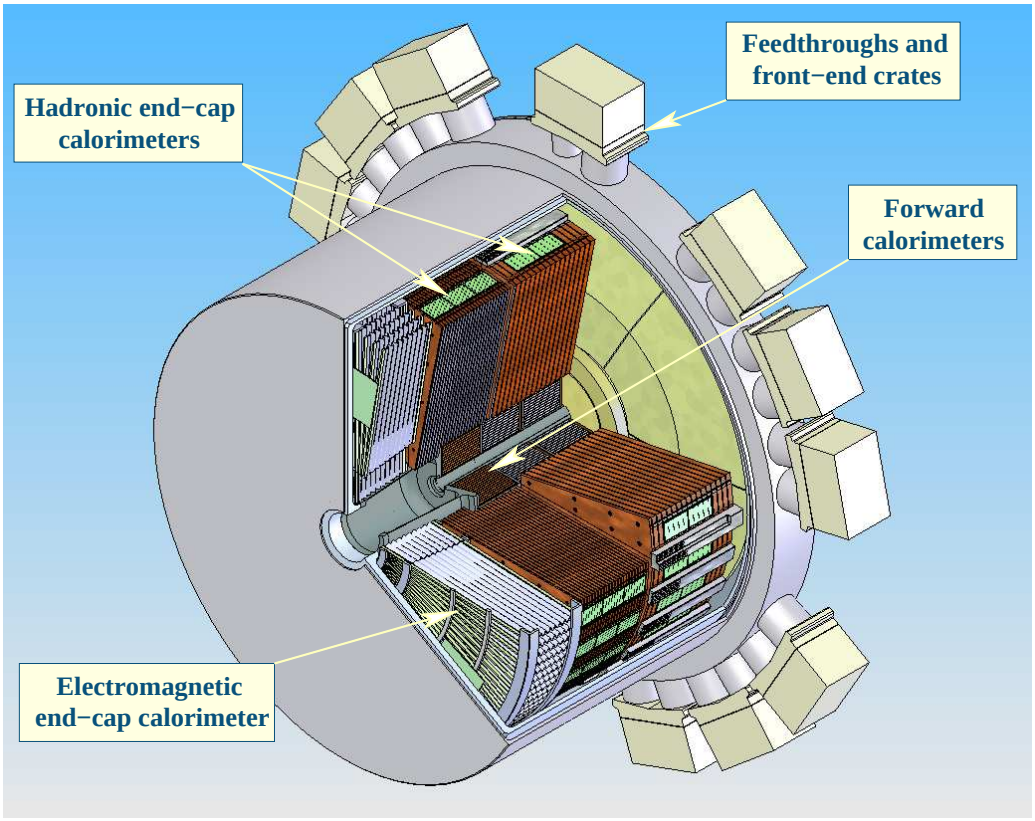

Figure 1. An artist's view of an end-cap cryostat with a cut-away showing the positions of the three end-cap calorimeters. The outer radius of the cylindrical cryostat vessel is 2.25 m and the length of the cryostat is 3.17 m

(EMEC) and forward (FCAL) calorimeters [3] (see figure 1). The HEC sits behind the EMEC and is completely shadowed by it.

The reconstruction of jets in the forward region and the measurement of the missing energy drive the performance parameters required. For the ATLAS hadronic calorimetry, the jet energy resolution is required to be of order $\sigma(E)/E = 50\%/\sqrt{E} \oplus 3\%$ (E in GeV) [4]. Such a resolution is sufficient for jet reconstruction and jet-jet mass measurements, as well as missing transverse energy measurements for the physics processes expected at the LHC.

Liquid argon is used as the active material in the ATLAS end-cap calorimetry. It was chosen because of its intrinsic linear behaviour, stability in response over time and, most important, its radiation tolerance. Approximately 12 interaction lengths are required to fully contain the jets from the 14 TeV proton-proton collisions at the LHC [5]. The total thickness of the material in front of the HEC calorimeter (EMEC calorimeter, inner tracker, etc.) is about two interaction lengths. The consequent 10 interaction length requirement for the HEC [4], combined with space and fiscal constraints, lead naturally to the choice of copper as the HEC absorber.

The HEC calorimeter consists of two cylindrical wheels in each ATLAS end-cap cryostat: a

[1] Pseudorapidity is defined as $\eta = -ln\,tan(\theta/2)$, where θ is the production angle with respect to the beam axis.

2007 JINST 2 P05005

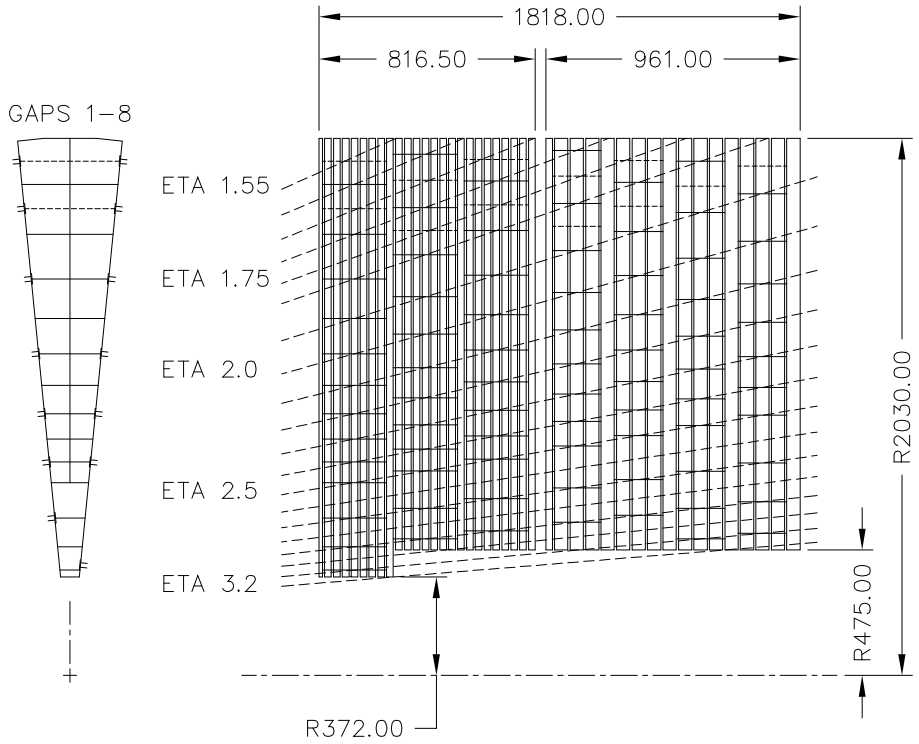

Figure 2. Schematic $r-\phi$ (left) and $r-z$ (right) view of the hadronic end-cap calorimeter modules. Note the semi-pointing layout of the read-out electrodes, as indicated by the dashed lines. Dimensions are in mm.

front wheel (HEC1) and a rear wheel (HEC2). The parameters of the wheels are summarized in table 1. Each of the four HEC wheels is constructed of 32 identical wedge-shaped modules (see figure 2). The HEC1 modules are made of 25 copper plates, while the HEC2 modules are made of 17 copper plates. The HEC1 (HEC2) copper plates are 25 mm (50 mm) thick, except for the front plates of both front and rear modules which are half-thickness plates. The gaps between the plates are 8.5 mm in all cases. The resulting sampling fractions of HEC1 and HEC2 for minimum ionizing particles [6] are 5.5% and 2.8% respectively. Both HEC1 and HEC2 have the same outer radius of the copper of 2.03 m. The wheels have an inner radius of 372 mm for the first 9 plates of HEC1 and 475 mm for the remaining 16 plates of HEC1 and all 17 plates of HEC2. The FCAL calorimeter fits inside this 475 mm inner radius, covering the region $3.2 < |\eta| < 4.9$.

High reliability is a necessary requirement, partly due to the difficulties of access to enact repairs, and so each liquid argon gap is subdivided into four drift spaces of about 1.8 mm by three parallel electrodes. The central electrode in each gap contains pad shaped electrodes defining the read-out cell structure as shown in figure 2, while the side electrodes serve only as high voltage carriers (see figure 3). This arrangement forms an "electrostatic transformer" with an EST ratio of 2. Each subgap has an independent high voltage connection and the nominal high voltage applied is 2000 V. Such a scheme has the same behaviour as a double gap of 4 mm, but without the drawbacks associated with a larger high voltage (which would be 4000 V) and greater ion build-up. High voltage is provided to the calorimeters through HV feedthroughs situated in the gas above the

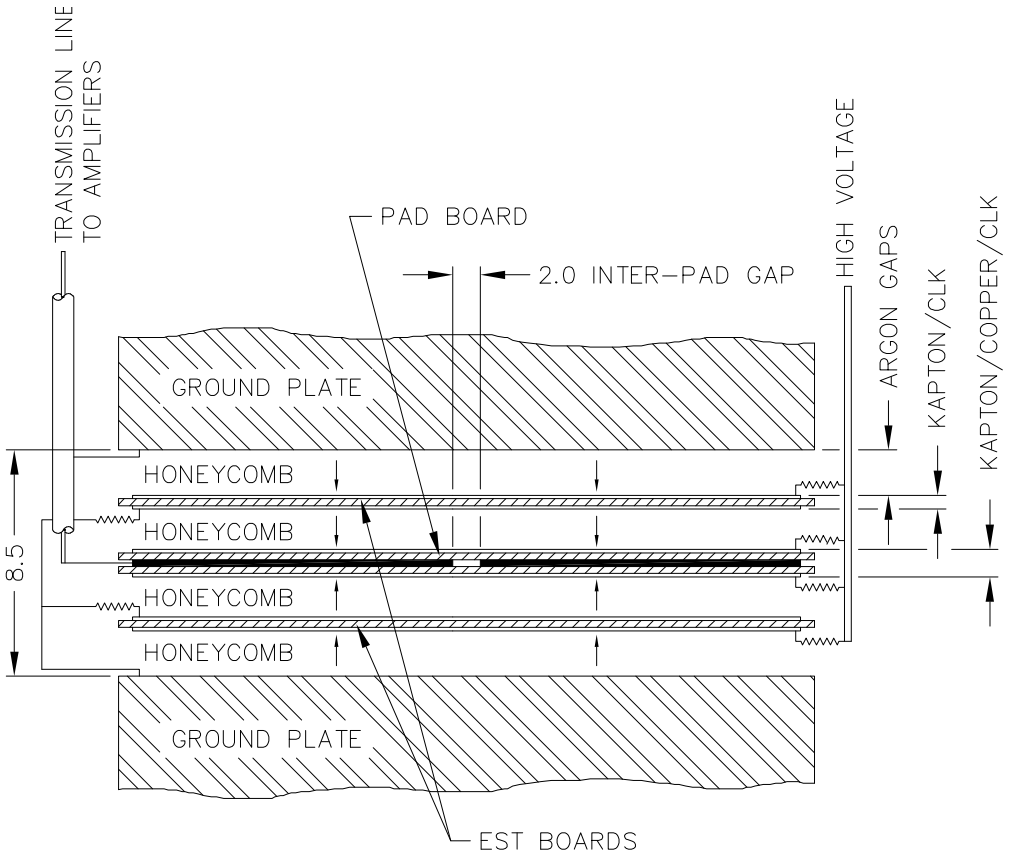

Figure 3. Schematic of the arrangement of the read-out structure in the 8.5 mm inter-plate gap. Dimensions are in mm.

Parameter	**HEC1**	**HEC2**
Number of wheels	2	2
Weight of each wheel	67,300 kg	89,900 kg
Number of modules per wheel	32	32
Gap between modules in azimuth	2 mm	2 mm

Table 1. HEC wheel parameters.

liquid argon in the main cryostat volume.

The transverse granularity of the read-out was chosen with the aim of reconstructing the decay $W \rightarrow jet + jet$ with high transverse momentum [4]. The size of the read-out cells is $\Delta\eta \times \Delta\phi = 0.1 \times 2\pi/64$ in the region $|\eta| < 2.5$ and $0.2 \times 2\pi/32$ for larger values of pseudorapidity. The arrangement of the read-out cells, defined by pads etched on the central foil in each gap, provides a semi-pointing geometry (see figure 2). To provide a good signal to noise ratio, especially for muons, the signals from cells paired in depth are amplified (using GaAs preamplifiers) and summed in the cold [7] prior to extraction of the signal through feedthroughs [8] to the calorimeter warm electronics situated in crates directly behind the feedthroughs. The signals are summed in

four read-out depths: HEC1 gaps 1–8, HEC1 gaps 9–24, HEC2 gaps 1–8 and HEC2 gaps 9–16. This segmentation in depth facilitates the identification of muons and provides information on the longitudinal shower evolution.

The paper is organized as follows. Section 2 first provides a general description of the HEC detector and then goes on to describe the manufacture of the main components necessary to construct a HEC module. This section also covers the actual stacking of the modules, as well as module prototyping. Section 3 describes the assembly of the modules into the four wheels and the insertion of the wheels into the cryostats. A description of the liquid argon purity and temperature monitoring instruments mounted on the wheels is included in this section. The tests of the assembled wheels, both while warm and cold, is the subject of section 4. Results from a series of beam tests of the modules are summarized in section 5. Finally section 6 reviews the "as-built" aspects of the calorimeters at the time of delivery to the ATLAS experimental cavern and section 7 offers conclusions.

2. Calorimeter description

The HEC wheels sit on rails, shared with the EMEC, in the end-cap cryostats. The design dimensions of the wheels and their locations in the cryostat are summarized in table 2. Note that it is anticipated that the cryostats will need to be a few mm further from the interaction point than designed, to allow the signals and services of the inner detector to be routed out between the barrel and end-cap cryostats. The HEC modules are held together in the wheel structure by copper tie bars between adjacent modules plates at the inner radius, and by stainless steel (type 316 or 304) connecting bars at the outer radius. The cold electronics are mounted between the connecting bars. The 32-fold symmetry in the wheel scheme is broken only by special connecting bars at the rail positions, which act additionally as sliders (see figure 4). The wheel structure created when the 32 modules are clamped together is quite stiff, and sagged by about only 0.3 mm when supported on the rails. To allow for handling and transport, the structure was designed to withstand 3.5 g before undergoing plastic deformation.

The parameters for the modules are provided in table 3. Each module of the HEC1 wheel is made with 24 8.5 mm inter-plate gaps and is read out in two read-out depths. The first depth is comprised of the front 8 gaps and the second of the rear 16 gaps. The HEC2 modules are each made with 16 8.5 mm inter-plate gaps and are read out in two 8-gap read-out depths. The structural strength of the front and rear modules is maintained by seven 12 mm and 16 mm diameter stainless steel tie rods, respectively, which pass through the plates and are bolted down with a tension such that the minimum pressure holding the plates together is equivalent to about three times the weight of the module. Annular spacers on the tie rods maintain the 8.5 mm gaps between the copper plates.

The HEC1 and HEC2 wheels are restrained within the cryostat such that the rear of both of the wheels is securely locked along the beam axis (z) during cool down. There are two main effects when the temperature of the wheel structure is reduced to liquid argon temperature. The first is the overall contraction of the wheels from the room-temperature state. The support rails are surface treated to provide a low-friction (coefficient of friction ~ 0.035) environment to allow the structure to slip laterally at the support points to accommodate the contraction. Guides located at the 12 o'clock position within the cryostat determine the position of the structure inside the cryostat. The

2007 JINST 2 P05005

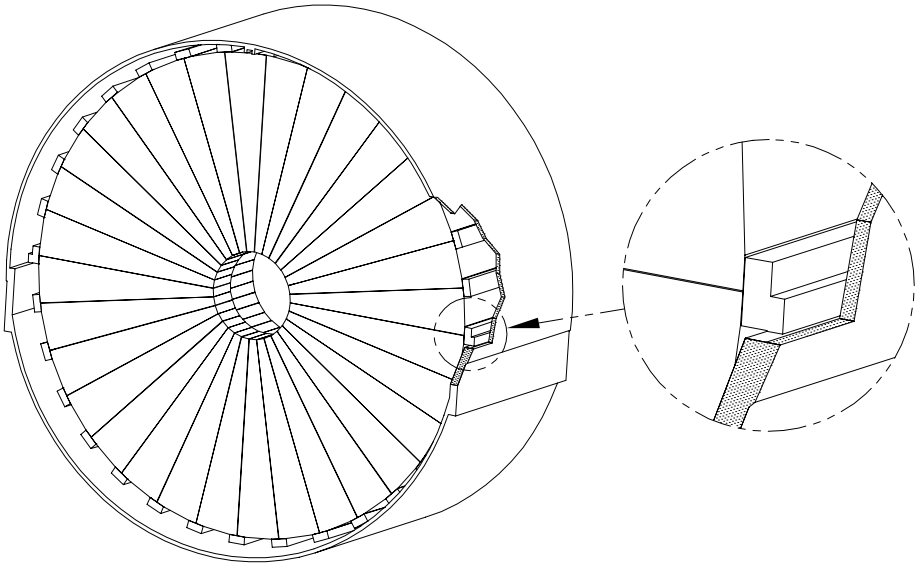

Figure 4. Schematic of the support of the HEC within the end-cap cryostat. The outer radius of the HEC (warm) is 2.09 m.

Parameter	**Value**
Z position of front of HEC1 (warm)	4,277 mm
Z position of front of HEC2 (warm)	5,134 mm
Length of HEC1 (warm)	816.5 mm
Length of HEC2 (warm)	961.0 mm
Outer radius of HEC (warm)	2,090 mm
Average clearance between HEC inner radius and cryostat tube containing the FCAL	15 mm
Outer radius of copper (warm)	2,030 mm
Inner radius of copper:	
Plates 1-9 front module (warm)	372 mm
All other plates (warm)	475 mm
Gap between copper of HEC1 and HEC2 wheels	40.5 mm

Table 2. Design locations and dimensions of the hadronic end-cap calorimeter. The z positions are with respect to the ATLAS interaction point.

second effect of the cooling is caused by the differential contraction (2.2×10^{-4}) of the stainless steel components relative to the copper plates. The clamping force of the various bolts is reduced by about 20% because of this. Care was taken during assembly to check the torque on bolts, so they would remain satisfactorily tight when cold. Temperature differences during cool down were restricted to 20 K, so as to limit thermal stresses to below 350 MPa.

The 8.5 mm gaps between the copper plates are instrumented with a read-out structure forming an electrostatic transformer (EST) [9] as shown in figure 3. This structure optimizes the signal-to-

2007 JINST 2 P05005

Parameter	Front modules	Rear modules
Number of copper plates	25	17
Thickness of first plate in module	12.5 mm	25.0 mm
Thickness of standard plates in module	25.0 mm	50.0 mm
Weight of standard plates	90 kg	180 kg
Module weight	2,103 kg	2,811 kg
Distance from copper plate to copper plate	8.500 mm	8.500 mm
Liquid argon subgaps	1.969 or 1.954 mm	1.969 or 1.954 mm
Honeycomb thickness	1.816 mm	1.816 mm
Total thickness of PAD and EST boards in gap	0.625 or 0.685 mm	0.625 or 0.685 mm
Number of read-out gaps	8+16 = 24	8+8 = 16
Number of read-out segments	2	2
Number of read-out towers	24+23 = 47	21+20 = 41
Number of preamplifier boards	3	2
Number of preamplifier chips	42	28
Number of low-voltage lines	12	8
Number of calibration distribution boards	1	1
Number of calibration lines	28	16
Number of high-voltage lines	4+4 = 8	4+4 = 8
Number of tie rods per module	7	7
Tie rod diameter	12 mm	16 mm
Tie rod stress	78 MPa	79 MPa
Tie rod thread root stress	125 MPa	118 MPa
Outside diameter of spacers for 8.5 mm read-out gaps	17 mm	23 mm
Maximum stress on the copper by the spacer	138 MPa	138 MPa

Table 3. HEC module parameters. All dimensions are nominal. The EST boards were manufactured at two separate production sites and have a different nominal thickness at each site (145 μm and 175 μm respectively).

noise ratio, while reducing the high-voltage requirement and ionization pile-up, and limits the effect of failure modes such as high-voltage sparks and shorts. The boards in the 8.5 mm inter-plate gap are of two types: a central board that contains the read-out electrode pads (hereinafter referred to as a PAD board) and two boards that are part of the EST (referred to as EST boards).

The EST boards were manufactured at two separate production sites. The boards produced at the first site (about 80% of the total) have a nominal thickness of 145 μm, whereas the boards produced at the second site are nominally 175 μm thick. Each EST board is made of a layer of insulator sandwiched between two high resistive layers of carbon-loaded Kapton®[2] (CLK). The CLK material has a nominal resistivity of 0.5 MΩ/square on the side facing the PAD board and 1 MΩ/square on the side facing the copper absorber. A PAD board, nominally 335 μm thick,

[2]Kapton® is a registered trademark and product of E. I. du Pont de Nemours and Company.

contains a layer of 35 μm thick copper etched with the pads of the read-out electrode structure.

The signals from the pads of this electrode structure are amplified and summed employing the concept of active pads: the signals from two consecutive pads in depth are fed into a single preamplifier, based on GaAs electronics. The use of cryogenic GaAs preamplifiers provides the optimum signal-to-noise ratio for the HEC. An important aspect of the HEC is its ability to detect muons, and to measure any radiative energy loss. The density of the electronics on the HEC wheels with their rather modest number of read-out channels (5632 in total) is such that the heating effect of the electronics on the liquid argon does not produce bubbling. This allowed the use of electronics in the liquid argon for the HEC, while a similar arrangement is not suitable for the EMEC. The output of the preamplifiers is summed on the same printed circuit board to produce one signal from each tower. The signal sent to the signal feedthrough for each tower is thus comprised of the amplified and summed signals of the 8 or 16 cells with the same η and ϕ within a read-out depth.

2.1 Module prototyping

An extensive programme of module prototyping and testing was performed before the final construction of the calorimeter. From the initial stage onward, this prototyping involved building full-size modules, using the facilities of all future assembly and plate machining sites, and also utilizing prototypes of the cold electronics. The full-size prototyping proceeded in three stages, an initial module -1 stage, followed by a module 0 stage, and finally a production stage. The initial module -1 design was described in detail in a technical design report [3]. Changes from module -1 to module 0 included improved side cabling, and changes to the internal radius. Changes from module 0 to production modules were very minor. During production all modules were cold tested, and about 25% were beam tested [10]. Two combined end-cap beam tests were undertaken, one with the HEC in combination with the EMEC in the region $1.6 < |\eta| < 1.8$, and one in the $|\eta|$ region around 3.2 covering the intersection of the EMEC, HEC and FCAL. Results from the EMEC/HEC combined test have been published [11], while the EMEC/HEC/FCAL data taken in summer 2004 are still being analyzed.

2.2 Module components

An extensive study of manufacturing procedures was undertaken to assure the final quality prior to starting any production of modules or sub-components. Over 1000 pages were written describing every production sequence in full detail. All procedures and tests were detailed, including the procedures to be followed when a non-conformance was detected. All production forms were agreed to by the HEC Group and where production of the same items occurred at more than one site, forms were rationalized between the sites. All forms were made freely available to the ATLAS collaboration, so as to obtain formal agreement from the collaboration that we were ready to start production, and production funds should be spent. When this agreement was reached, the ATLAS Technical Coordination Group enacted a formal Production Readiness Review (PRR) and an Activity Status System Overview (ASSO) which reviewed these documents and the management structures which would oversee production and assure quality.

After completion of production, the various important measurements recorded during this production were reviewed. A report detailing the “as built parameters” of the HEC was produced [12],

2007 JINST 2 P05005

which analysed the effect of variations in production quantities, such as copper plate thickness, on calorimeter performance. On the basis of this study, the important module production measurements were recorded in a module production database. This database has been transferred to the ATLAS database group, so it can be up-kept along with databases from other ATLAS sub-detectors.

2.2.1 Absorbers

The 25 (17) copper plates that make up each HEC1 (HEC2) module are designed in two radial sizes. The first nine plates of the HEC1 modules, which do not encompass the FCAL, are larger than the other plates. The plates were cut and finished in machine shops in Canada and Russia. Stringent quality control, using custom designed tooling, was undertaken to confirm machining was to specification. All critical dimensions were entered into a database. After machining, the plates were cleaned in a bath to remove machining oils. This bath had a mild inhibitor to slow subsequent oxidization. At some sites, a commercially available detergent based cleaning agent was used in conjunction with an ultrasonic bath, while at others an alkali solution (with pH = 11–12) at 50–55°C was used. All holes were individually cleaned. Immediately after cleaning, the plates were washed in a clean water bath and dried. The plates were subsequently inspected for cleanliness and for any potential source of metal slivers or shavings. No difference was observed between the two cleaning methods as far as the resulting argon purity was concerned, but one item of note was that the chemically cleaned plates remained more reflective and appeared to oxidize more slowly.

All plates have notches on both sides for wiring. To keep machining costs to a minimum, the modules were designed to have a minimum number of signal cable notches, all with the same width. Thus each notch carries the signal lines from two sets of radially adjacent electrodes. Seven major different copper plate profiles were used to maintain the semi-pointing geometry in η. There are some minor differences in ϕ, resulting in a total of 22 profiles. The plate thickness tolerance was 0.050 mm; the flatness tolerance was 0.5 mm for the 25 mm plates and 0.25 mm for the stiffer 50 mm plates. Each plate has seven holes in it to accommodate the tie rods. The material of the 25 mm plates is quarter-hard copper while the 50 mm plates are hot-rolled copper. In order to limit the possibility of producing copper slivers when attaching fasteners to the copper plates, and to increase the pullout strength, threaded bolt holes were equipped with stainless steel threaded inserts at all mechanical fastening locations. The 25 mm copper plates each weigh about 90 kg and the 50 mm plates about 180 kg, and so the plates had to be handled using a crane. To facilitate this operation, two small dimples (about 1 cm in diameter and 0.5 cm deep) were machined on both inter-module plane edges of the plates. The plates could then be lifted in the horizontal orientation using two clamps that fit into the dimples. In this way the plate could be handled easily and safely during all operations: cleaning, inspection and stacking.

2.2.2 Honeycomb spacer mats

Honeycomb insulating spacing mats maintain the gaps between the PAD and EST boards and between the EST boards and the copper plates, while still allowing the nominal high voltage to be maintained across the gaps. The nominal thickness of the honeycomb is 1.816 mm with a manufacturing tolerance of ± 0.203 mm.

2007 JINST 2 P05005

The honeycomb was received cut to thickness in rectangular sheets from which six pie-shaped sheets were cut using a steel-rule die cutter. Just prior to use in a module, each honeycomb layer was vacuumed and then placed between two metal plates and checked for high-voltage standoff at 2500 V. The pass criterion for this test was that the honeycomb must draw less than 5 nA at 10% relative humidity (H_{rel}). To allow this test to be done at different ambient levels of humidity, the average leakage current (i_{leak} in nA) was studied as a function of humidity and found to be empirically described by:

$$i_{\mathrm{leak}} = e^{-1.81+0.106H_{\mathrm{rel}}}$$

Honeycomb layers drawing more than approximately 10 times the average leakage current at the ambient humidity were rejected.

As the honeycomb was manufactured from large blocks and these blocks were made in a normal factory environment without particular care for cleanliness, there was a concern that conducting foreign material might be present in the blocks. For this reason, every pie shape was labeled with a unique serial number. No evidence was found for such conducting foreign material. However, a random sampling of the weight of the pie sections was performed to determine the variation of the fraction of argon displaced by the honeycomb. The sampling showed that the aramid resin thickness varied smoothly from one end of a honeycomb block to the other. This was anticipated as in the manufacturing process the aramid fibre honeycomb block is dipped in a phenolic resin bath and dried without rotating. Hence the resin tends to flow down the honeycomb tubes prior to setting. The RMS variation of the weight of the honeycomb pies used was 6.4%. This variation causes a variation in the amount of liquid argon in the gap, which leads to an estimated variation in the signal in a read-out tower of 0.21%. The thickness of the honeycomb mats was measured to be on average 1.923 mm, with an RMS variation of 0.037 mm.

2.2.3 Electrodes

The PAD boards and EST boards are made of only four primary components, namely polyimide, epoxy sheet glue, rolled copper, and carbon-loaded polyimide. Figure 5 shows the structure of the PAD and EST boards, together with the pre-manufactured composite sheet materials used in the assembly.

The EST boards were manufactured at two separate production sites. As the epoxy sheet glue has a limited shelf life, it was procured from local suppliers and was not available with the same thickness at the two sites. About 80% of the EST boards were manufactured with 10 μm sheet epoxy, the rest with sheet epoxy 25 μm thick. All other materials were purchased from a single supplier.

The carbon-loaded polyimide is manufactured by DuPont™[3] under the trade name Kapton® XC. The company supplied the collaboration with a product having approximately 60% RMS variation in resistivity. The product was purchased in 25 μm thickness and has mechanical properties similar to polyimide. The volume resistivity of the material is about 24 kΩ mm, which gives rise to a small resistance in series with the capacitance of the gap.

The read-out structure is etched in the central layer of the PAD board on the 35 μm thick copper. The arrangement of the copper pads, as shown in figures 2 and 6, provides a semi-pointing

[3] DuPont™ is a trademark of E. I. du Pont de Nemours and Company.

2007 JINST 2 P05005

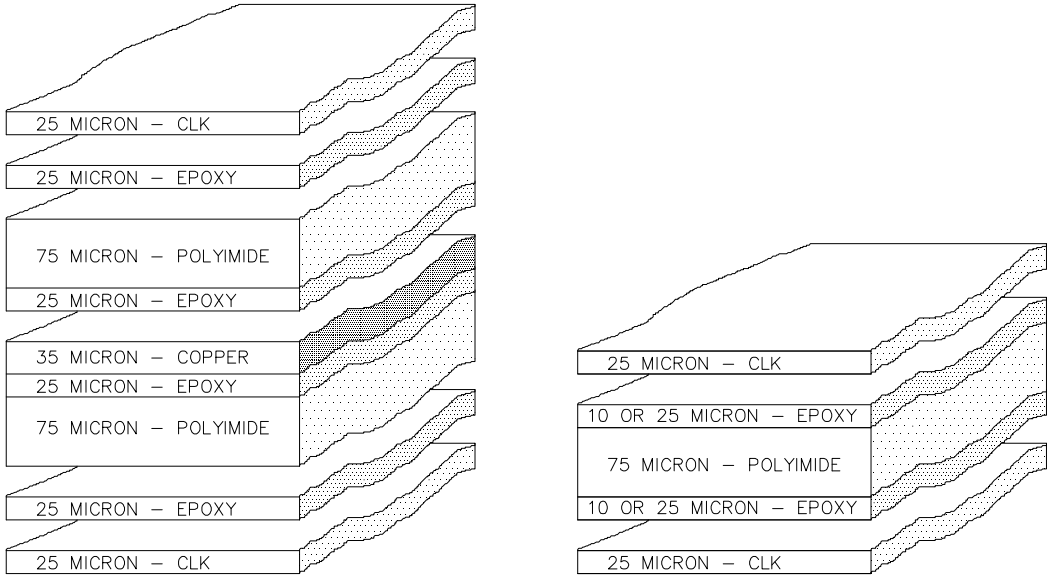

Figure 5. Cross section of PAD board (left) and EST board (right). EST boards were manufactured at two sites. One site used 10 μm sheet epoxy and the other site used 25 μm sheet epoxy.

geometry since the etched pads are identical for several gap depths, before making a step to reflect the $z = 0$ pointing η geometry. This allowed the production costs to be limited, because only seven different pad patterns were used. The pointing cell structure points at the nominal interaction point when the modules are warm, and at a point 15.2 mm closer to the end-cap when cold.

The high-voltage and ground connections to the resistive polyimide are made by inserting a small copper-clad polyimide tab between the resistive polyimide and the first glue layer (see figure 7). Two such connections are made, to provide redundancy in the connection, one at the outer radius of the board and one on the side of the board near the inner radius.

All materials requiring alignment in the boards were pre-cut with a steel rule die. To manufacture the boards, the required materials are aligned in a press and taken through the temperature cycle required by the glue. Care had to be taken that all materials were pre-cut and aligned at a well defined humidity, as polyimide displays a strong dimensional variation with humidity. With tolerances of about 1 mm, this required that we only cut and baked materials when the relative humidity was below 50%. Typically ten boards were made in the press at each baking, and the wastage rate was a few percent.

To assure uniformity, all PAD boards were produced at a single site. Key to the assembly was the alignment of the etched copper-clad Kapton® pad array within the board. For this purpose, six alignment crosses were etched around the periphery, outside the area of the final pad array. Precision holes were punched in each sheet using the alignment crosses as a datum reference. The same six external alignment holes were made on all the components of the board. PAD board assemblies were typically processed in batches of ten units in a custom designed press. The press was equipped with six alignment dowels to match the punched holes of the pad board layers. When

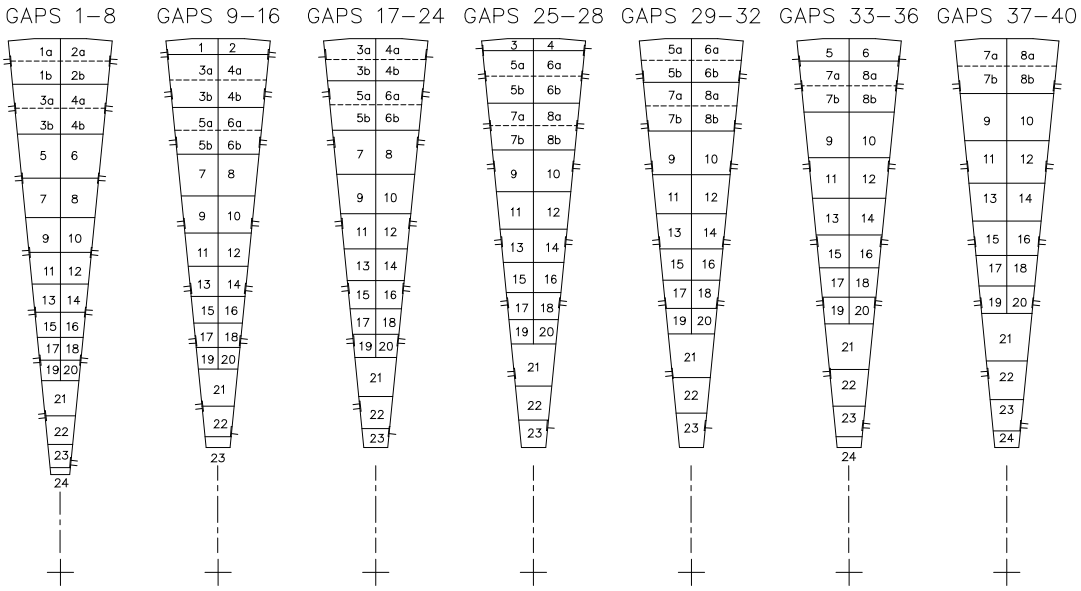

Figure 6. Drawing of the seven PAD board electrode structures. Note that electrodes labeled a and b, and separated by dashed lines, are summed in the cold and read out as single towers. The outer radius of all the PAD boards is 2030 mm. The inner radius of the PAD boards in gaps 1–8 is 373 mm and is 473 mm for all the other PAD boards.

filled, the press typically comprised of:

1. Aluminium strengthening bars
2. Alumimium plate
3. Air pillow at 20 atmospheres pressure
4. Ten layers of:
    a. Rubber sheet
    b. Glass filled Teflon sheet
    c. Teflon sheet
    d. Materials of pad board (including glue)
    e. Teflon sheet
    f. Glass filled Teflon sheet
5. Rubber sheet
6. Aluminium plate
7. Aluminium strengthening bars

Once the oven had passed through its temperature cycle consisting of an initial one-hour heating phase, a five-hour slow baking phase during which the temperature rose from 110°C to 145°C, and an overnight cool-down, the oven was opened and the cooled pad boards removed. The final step was then to cut the final outline using a steel rule die with the pad board positioned on the die by dowels at the six alignment hole locations.

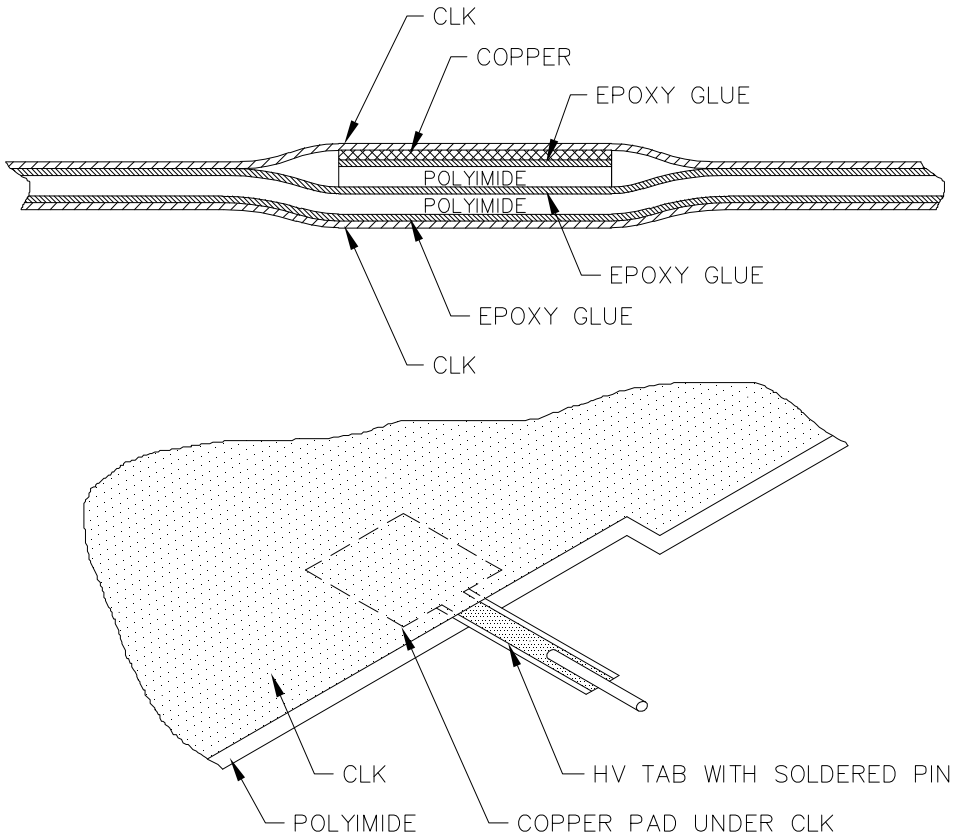

Figure 7. Sketch of the high-voltage connection. A pin is soldered to the HV tab to connect to the HV strip line connector. The width of the HV tab is 4 mm.

The production of the EST boards was rather similar to that of the PAD boards, except the EST boards are thinner and the variation in thermal behaviour between the various components is much less. EST board production therefore was technically slightly less demanding than PAD board production, but since twice the number of boards were required to be manufactured, it was the more manpower intensive task. For this reason, production was shared between two institutes. The local procurement of the sheet glue resulted in differences in thickness between the finished boards, but other than this issue, the production was very similar at both sites. Indeed the central part of the tooling, the glue press, was identical at both sites.

The procedure for the final quality control of the EST and PAD boards after production was similar. The resistance between the two high voltage connections was measured to check that they were both operational. The resistance was recorded in the database. The board was then visually inspected and underwent a HV check, prior to storage for subsequent use in module stacking.

The measurement and recording of the resistance was important for two reasons. This resistance is an indirect measurement of the resistivity of the carbon-loaded Kapton®, which affects the signal crosstalk between adjacent read-out towers and the voltage drop across the liquid argon gap when currents flow in the HV system. The average signal crosstalk was estimated to be about 1.5% and this estimate has been confirmed by measurement. As the crosstalk depends on the

carbon-loaded Kapton® resistivity, the knowledge of the resistivity is key to the ability to correct for this effect. At high LHC luminosity, the currents in the carbon-loaded Kapton® will cause a significant voltage drop which will result in a reduction of the electric field in the liquid argon and hence diminish the measured signal. This signal reduction is estimated to be on average 0.15%, at the highest LHC luminosity, with an RMS variation of 0.06%, but will depend on the resistivity.

2.2.4 Tie rods and spacers

The plates within the modules are held together with seven tie rods. Annular spacers on the tie rods maintain the 8.5 mm gaps. The parameters of the tie rods and spacers are summarized in table 3. In the front modules these spacers have a 17 mm outside diameter, and in the rear modules a 23 mm outside diameter. This feature enables the distribution of the tie-rod tensile load, plus the weight of the front module absorber plates, to be carried by the lower module plates comfortably within the yield strength of the copper material. The slight increase in the spacer diameter in the rear module is to allow enough force to be applied on a minimum of three spacers to flatten the stiffer 50 mm copper plates.

2.3 Module mechanical assembly

Modules were assembled in clean rooms at stacking sites in Canada, Germany and Russia. All modules were stacked on a stacking table that contained alignment bars that assured the plates were aligned correctly.

The module stacking process started by placing the rearmost plate on the stacking table along with the 7 tie rods, that are bolted to this rear plate (see figure 8). The components of the rearmost gap: 4 honeycomb sheets, 2 EST boards and 1 PAD board, then had their final individual HV tests performed prior to stacking. Each of these components was then lowered into place over the tie rods. When all the components of the gap were in place, the operation to lower the next copper plate into place was started. Just prior to being put in place, the top EST and honeycomb were inspected for copper slivers that could have been produced during this lowering procedure. Once in place, the gap was tested to 2000 V for 2 minutes to provide assurance that no conducting material was present. During this procedure, the currents from all four liquid argon subgaps were monitored along with the humidity. Gaps that failed this procedure were re-stacked with new honeycomb placed in the failed subgap. This procedure was repeated until the module was fully stacked.

Once a module had been stacked, the HV side wiring harnesses were installed and a two-day test at 1800 V performed. After this test, the lengthy procedure of installing the signal wiring on the side of the modules was undertaken. Finally a ten day test at 1800 V was performed (see figure 9), prior to declaring the module ready for preparation for shipment to CERN.

Since it was possible that some plates might have shifted during the shipping, on arrival at CERN all modules were checked in a go-no-go device that assured the modules were geometrically suitable to form part of a wheel. If this were not the case, the tie rods were loosened and adjustments made. The small manufacturing variations in the envelope of the modules allowed by this procedure were taken up in the assembly of the wheels by slight variations in the 2 mm inter-module gap. The RMS variation of this gap was measured to be 0.53 mm.

A total of 134 HEC modules were assembled and all were cold tested in liquid argon at CERN as part of their quality control (QC) acceptance. To pass this cold test, there had to be either

2007 JINST 2 P05005

Figure 8. Stacking table with a partly stacked module. The module assembler is shown carefully lowering a EST board onto the 7 vertical stainless steel tie rods. When completed this front module will consist of 25 copper plates, with 24 8.5 mm gaps filled with the honeycomb/electrode structure.

no shorts, or a single short that was removed in the warm by removing a foreign object, or by disconnecting a single HV subgap. Of the 128 modules selected to be installed in the ATLAS detector, 26 had one subgap disconnected, out of a total of 10240 subgaps. Of note is the fact that 21 of the 26 shorts were in subgaps between the EST and the copper. It is assumed that this indicates the majority of shorts arose from copper slivers coming from the copper plate that forms one face of these gaps.

The total of 134 manufactured HEC modules includes three spare front and three spare rear modules so as to allow module testing after assembly of the full wheels. The spare modules are currently in storage.

3. Calorimeter wheels

During the wheel assembly, each module had to pass HV tests once again, as well as capacitance control tests, electronic cabling and full signal reconstruction tests. These tests were repeated after the wheel assembly, after the wheel rotation, after the wheel insertion and finally after the full cabling of the HEC front and HEC rear wheels inside the cryostat. Figure 10 shows a HEC wheel fully assembled on the assembly table.

2007 JINST 2 P05005

Figure 9. Module undergoing a long term HV test at 1800 V for 10 days. The module is bolted on its shipping frame, and stored in a clean area or box. The relative humidity is monitored as well as the currents in the liquid argon subgaps.

3.1 Wheel assembly

The assembly of the four HEC wheels and their subsequent insertion into the end-cap cryostats, took place in a purpose-built clean room at CERN. For ease of assembly, the wheel was constructed on a purpose-built assembly table in the horizontal plane. The absence of a crane capable of lifting the table and an assembled wheel together dictated that the wheels be constructed at a height above the floor which would coincide with the 4080 mm centre height of the awaiting cryostat. Custom designed tooling was manufactured to provide a support stand with hydraulic height adjustment, which in turn provided support for the main wheel assembly table. The support stand also provided fastenings for a removable cantilevered catwalk to allow access to the wheels during the assembly procedure.

The 32 wedge-shaped modules comprising a complete wheel were assembled one to another in a horizontal orientation. The modules for each wheel were prepared for installation in batches of four, each one mounted on a purpose-built transportation trolley designed to carry the 3 tonne maximum load. The initial testing of each module ensured its electrical integrity prior to being released for installation in the wheel.

The two sliders, which would eventually support each wheel on rails inside the cryostat, are an integral part of the connection bar system which maintains the mechanical integrity of the wheel

2007 JINST 2 P05005

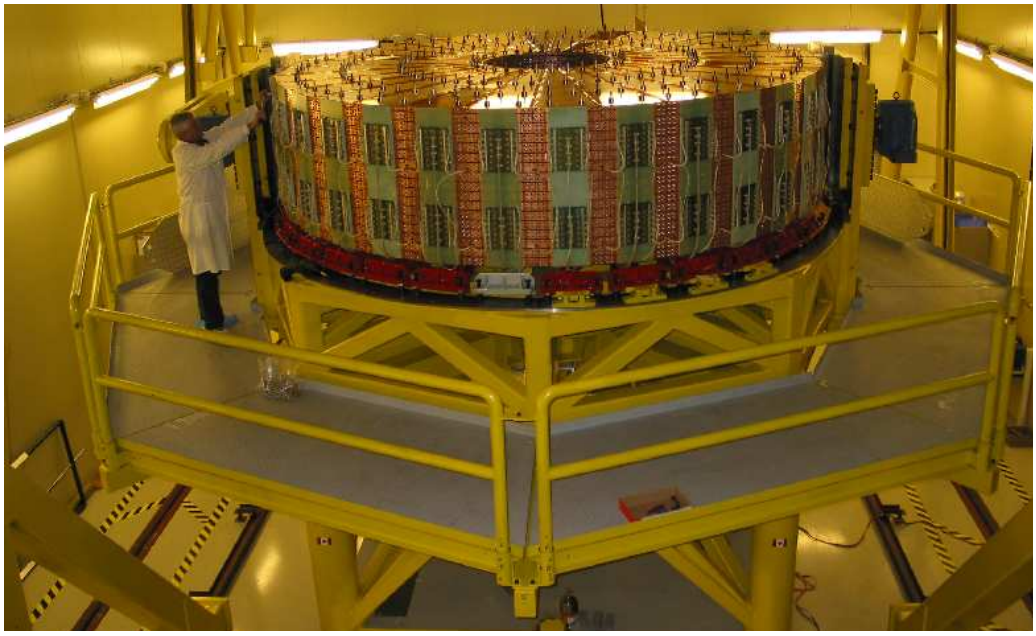

Figure 10. A HEC wheel fully assembled on the assembly table showing the "active pad" electronics.

structure. These two sliders are also the datum surfaces defining the origin of the wheel geometry and were therefore the first components to be positioned on the assembly table. The first group of four modules was assembled as two pairs, one pair at each of the two slider locations. The pairs were aligned, fastened, and bolted to the assembly table to act as an alignment reference for all subsequent modules. Assembly of the wheel proceeded at equal rates on each half of the assembly table. A pair of datum modules and their associated slider can be seen in figure 11, together with one of the two temporary wheel support rails which is bolted to a plate on the wheel rotation tooling.

Every module came mounted on a shipping frame which eventually would become an integral part of the assembly table. Each frame was designed with features to enable the adjustment of height, radial spacing and perpendicularity, and once this had been completed, the ability to bolt the frame and module to the assembly table. Consistent monitoring of the 2 mm inter-module gaps, coupled with the precise leveling of each new module, made the insertion of the final module in each half-wheel a relatively easy task. As can be seen in figure 12, the actual space between adjacent modules was actually controlled by the spacing of connection bar key slots in the copper absorbers.

With all modules having been installed and initially aligned, the final process was to verify the alignment and make fine adjustments where necessary to ensure trouble-free fitting of the connection bars at the outer radius of the wheel. Particular care was exercised because the signal cable harnesses exit the modules at the outer radius and enter into machined slots in the connection bars. Experience had proved that the fitting of connection bars should be performed one at a time, and an electrical test to determine signal line continuity and high voltage integrity be performed prior to the addition of an adjacent bar. Advantage was taken of the high-quality plate machining

2007 JINST 2 P05005

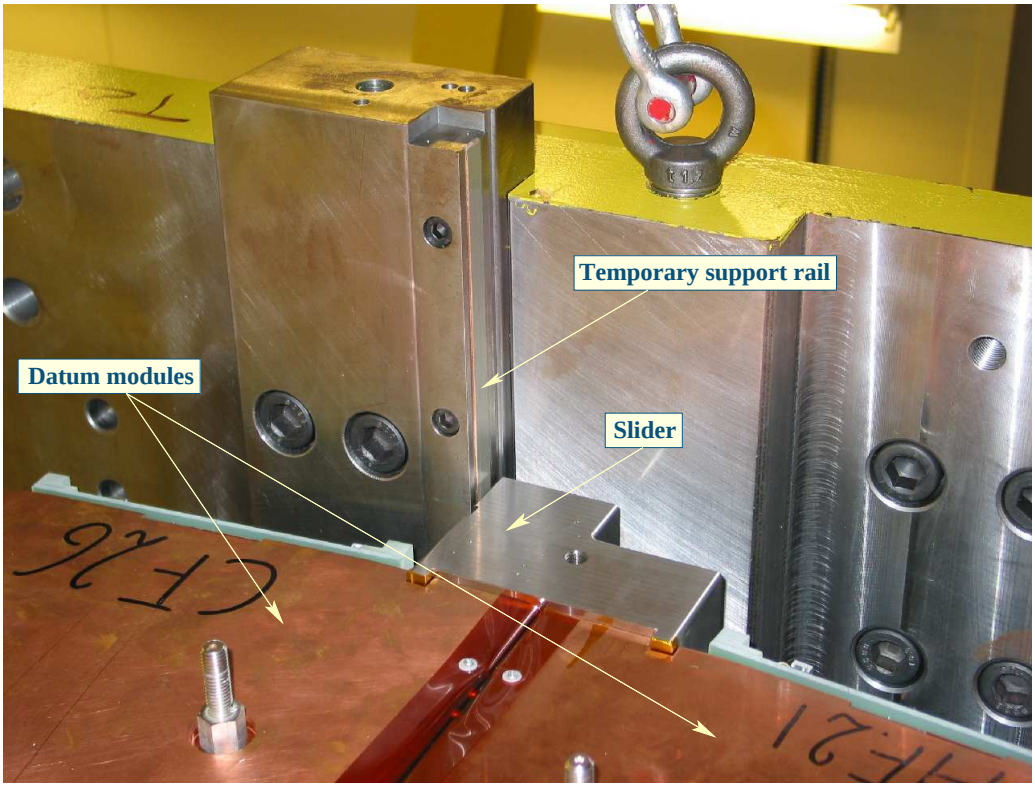

Figure 11. A pair of datum modules and their associated slider. One of the two temporary wheel support rails, which are bolted to plates on the wheel rotation tooling, can also be seen. A schematic of a wheel supported in the cryostat is shown in figure 4, together with a blow-up of a slider and a support rail.

which obviated the need to use any adjustment shims between the connection bars and the absorber plates. The final step in the assembly sequence was the fastening of the numerous copper tie-bars to the inner bore of the wheel. Any plate tolerance misalignments were compensated with the position-adjustable copper tie-bars.

3.2 Wheel rotation

Wheel orientation for cryostat insertion was required to be in the vertical plane. Special tooling was designed to raise the combined 100 tonne maximum load of wheel and assembly table, and then rotate it through ninety degrees. The multi-purpose, custom designed rotator, riding on four air pads, also served as a wheel transportation device to move from the wheel assembly area to the insertion bench attached to the open face of the cryostat. The air pad system was supplied with bottled air at a nominal pressure of 15 bar, and to facilitate ease of movement on the epoxy coated floor surface, the path of the air pads was coated with a thin layer of silicon oil.

Rotation of the load was achieved with the use of a heavy duty, motor-driven, ball-screw linear actuator controlled to allow a stepped, five-speed rate of travel. Extended to its full length when the table was horizontal, the actuator pulled on a lever arm connected to the table assembly via a splined shaft. A design feature allowed the point of rotation to be adjusted to match the centre of gravity of each of the two wheel types. A point approximately 10 mm above the theoretical centre

2007 JINST 2 P05005

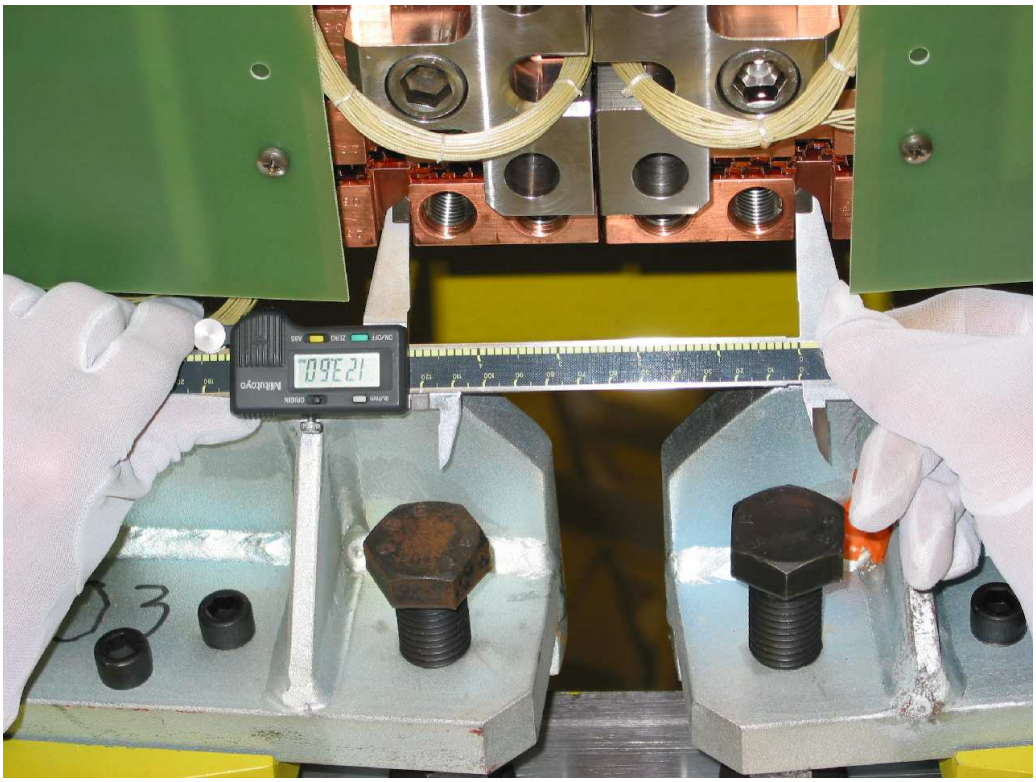

Figure 12. Final adjustment of module-to-module spacing, prior to installing the connection bars on the outer diameter of the detector wheel.

of gravity was chosen as a rotation point to minimize the load on the actuator and also to eliminate any chance of the wheel tending to "roll over" on reaching the vertical plane. Figure 13 shows the first of the four wheels being rotated into the vertical position.

Load transfer of the wheel to the cryostat insertion bench was achieved with the use of the hydraulic cylinder component of the air pad system. The vertical wheel was raised sufficiently to allow the assembly to pass over the insertion bench supports. Upon reaching end stops, the wheel was lowered and the temporary wheel rail plates, seen closest to the wheel in figure 13, were fastened to the bench. The rotator and the assembly table were then free to be withdrawn in preparation for the mounting of the insertion "push-pull" device.

3.3 Alignment measurements (including gaps)

The HEC wheel assembly table provided a central array of 32 datum location pins to ensure geometric precision of the wheel. In addition, the measurement and final adjustment of the inter-module spacing for connection bar installation guaranteed very accurate radial positioning of the modules.

Two precise alignment measurements of the module array were made on each of the four HEC wheels at different stages of construction and installation. The first survey was performed immediately after completion of the wheel on the assembly table. Optical targets were placed in special holders mounted on the front faces of the connection bars and a full survey of these points

2007 JINST 2 P05005

Figure 13. One of the two HEC1 wheels being rotated to the vertical orientation with the custom designed tooling after having being moved from the wheel assembly area. The wheel assembly stand can be seen on the left.

was recorded. The nominal 2.0 mm inter-module gaps were also measured at the inner and outer diameters, both on the front and rear faces of each wheel. Analysis of this measurement shows that the average gap was 2.16 mm with a 0.53 mm standard deviation. The distance across the outer faces of the sliders was recorded to ensure it was within the design envelope requirements, and also for comparison after the wheel had been rotated to check for any physical distortion of the wheel. No significant distortion was ever noted.

A second survey was performed after the wheel had been rotated, disconnected from the assembly table, and with the entire weight of the wheel being carried on the horizontal sliders. At this stage, the survey gave an accurate indication of any wheel distortion that may have occurred during rotation to a vertical orientation. By using the most upper and lower connection bar positions to determine any vertical deformation of the wheel structure, the average sag of the centre for the four wheels was measured to be 0.3 mm. These same survey target positions also verified the vertical

2007 JINST 2 P05005

Figure 14. A view showing technicians assembling the wheel alignment key prior to wheel insertion into the cryostat.

wheels remained perpendicular to their axes within ± 1.0 mm. Utilizing a photogrammetric survey technique, the survey data from the front face of the wheel was transferred to a similar optical target array on the rear face. The rear face survey data was used to determine the correct final machining of the wheel alignment keys, shown in figure 14, prior to insertion into the cryostat. This same rear face array was then used in conjunction with the cryostat alignment target array to determine the actual wheel position inside the cryostat, relative to external targets on the outer vessel wall.

3.4 Wheel insertion into the cryostats

After rotation, the wheels were placed on a support stand in front of the cryostat. According to the integration procedure, the pre-sampler detector and the EMEC wheel were inserted into the cryostat first, then the HEC front and rear wheels followed. Finally they were cabled and tested before closure of the cryostat (see section 3 above). This situation is shown in figure 15.

The wheel support rails inside the cryostat were fitted with a 15 mm wide strip of low-friction Permaglide®[4] rail adhered to a G10 insulating shoe. This low-friction rail was extended in a simpler form beyond the cryostat to the insertion bench, terminating at the temporary support rails delivered with the wheel. These in turn were also fitted with their own Permaglide® strips. The mating rails, fitted to the HEC wheels, were machined from an austenitic stainless steel with

[4]Permaglide® is a registered trademark and product of Kolbenschmidt Pierburg AG.

2007 JINST 2 P05005

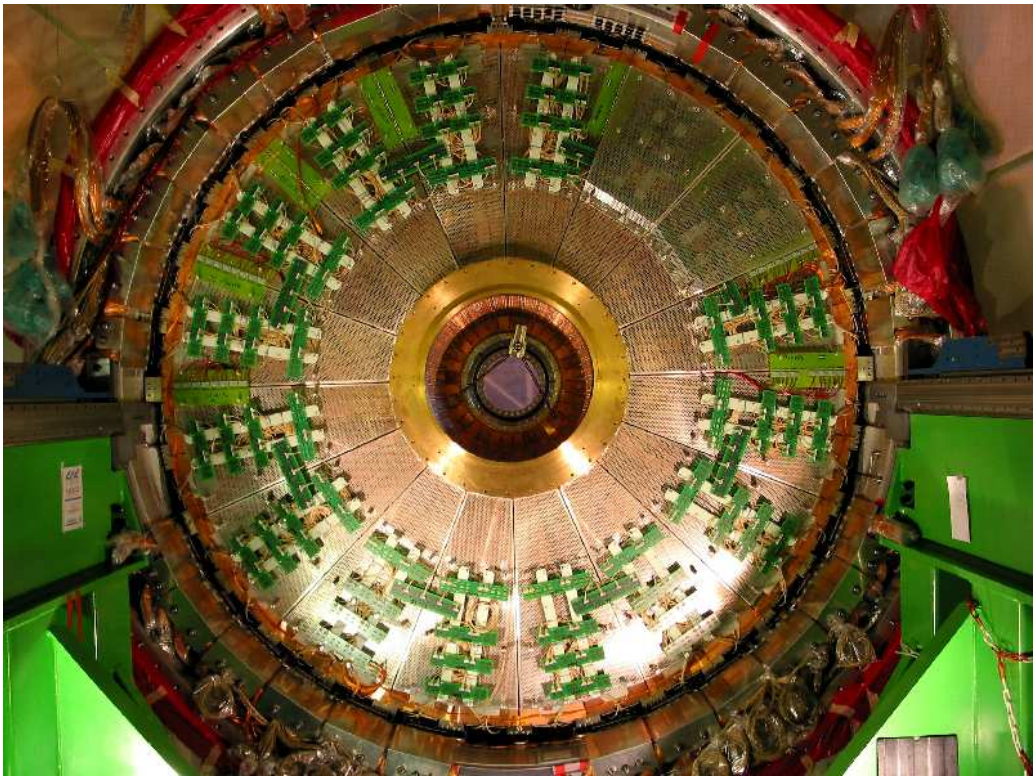

Figure 15. One of the end-cap cryostats fully loaded with calorimeters and electronics showing on the rear HEC wheel.

the sliding surfaces polished to remove all machining marks. The resulting coefficient of friction between the stainless steel and the Permaglide® strip was approximately 0.03.

An electrically powered insertion device, on loan from the H1 group at DESY, was used to push the wheels into the cryostat at an approximate speed of 1 mm/s. The maximum stroke was 300 mm; therefore, a system of steel spacer columns were used to increment the wheel into the cryostat. The insertion procedure was to push each wheel to within 500 mm of the cryostat face and at that point perform a transverse adjustment to align the top guidance key of the wheel to the mating key-way of the cryostat. Guide rails were adjusted to maintain this alignment until the key engaged with its key-way. Insertion continued under intense scrutiny to ensure there were no conflicts with associated cables or problems with the Permaglide® rail material. Forward motion was restricted by internal stops mounted to the wall of the cryostat. The insertion device was equipped with a load cell to prevent an overload condition at the wheel/stop interface.

3.5 Monitoring instruments

3.5.1 Liquid argon purity monitors

Electronegative impurities in the liquid argon reduce the collected charge and can degrade the performance of the calorimeter. At an impurity level of 0.5 ppm O_2-equivalent, an increase of 0.1 ppm will change the response of the ATLAS calorimeter by 0.1%. In order to ensure a stable operation, three purity monitors have been installed in pockets in the rear plates of each of the

2007 JINST 2 P05005

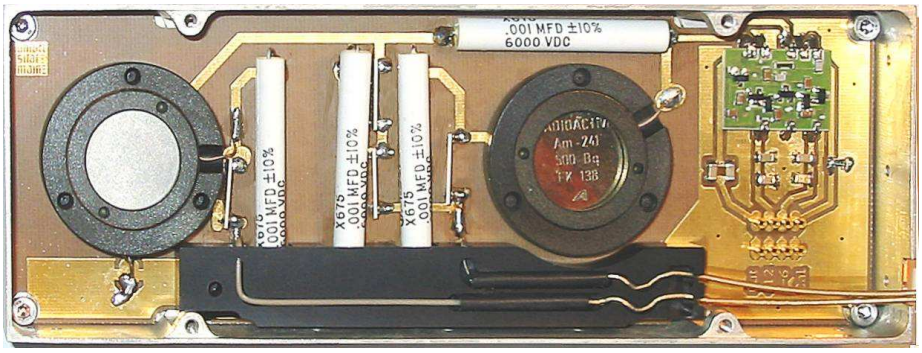

Figure 16. The liquid argon purity monitoring device in its shielding box.

hadronic end-cap wheels (six monitors per end-cap). Two of the three monitors are positioned at the outer radius of the wheel at the 12 and 6 o'clock positions. The third monitor is located at the 3 o'clock (9 o'clock) position in the case of the front (rear) wheel.

The concept of the impurity determination is based on the deposition of a known energy in the liquid argon using radioactive sources. The ionization charge is collected by an electric field and measured by a cold preamplifier. Each device consists of two radioactive sources: an ^{241}Am source provides 5.5 MeV α-particles and a ^{207}Bi source 1 MeV electrons from conversions.

The setup of the monitoring device is shown in figure 16. It consists of two separate liquid argon gaps for the collection of signals from the two sources, high voltage filters and distribution circuits and a single charge sensitive preamplifier[5]. The mechanical structure is made out of polyimide. Both signals (of the order of 2–4 fC) are read out by the preamplifier at the same time. The source of the signal is given by its polarity.

In order to extract the absolute oxygen content in the liquid argon, the ratio of the measured charges $Q_{\mathrm{Bi}}/Q_{\mathrm{Am}}$ is utilized. It is possible to use this ratio because the dependence of the charge on the impurity level is different for the two sources. An empirical calibration of the signal ratio of the two sources has been performed and the result is shown in figure 17. The obtained parametrization as a function of the temperature and the field strength has a total error of 15% on the absolute level of the oxygen content. Relative changes can be measured with a high precision of better than 10 ppb O_2-equivalent contamination. More details about the methods used and the performance of the devices can be found in [13].

3.5.2 Temperature probes

The usage of temperature probes in the HEC calorimeters is motivated by the necessity to measure temperatures while cooling down or warming up the detectors positioned in the cryostat and to monitor the liquid argon temperature during the operation of the detector at the LHC, since the drift velocity of the electrons is temperature dependent. The same probes have been used on all detectors in all three ATLAS cryostats.

During cool down (300 K to 88 K) the probes are used to monitor temperature differences between the different parts of the calorimeter. Excessive temperature differences can cause mechan-

[5]Preamplifier developed and provided by V. Radeka, Brookhaven National Laboratory.

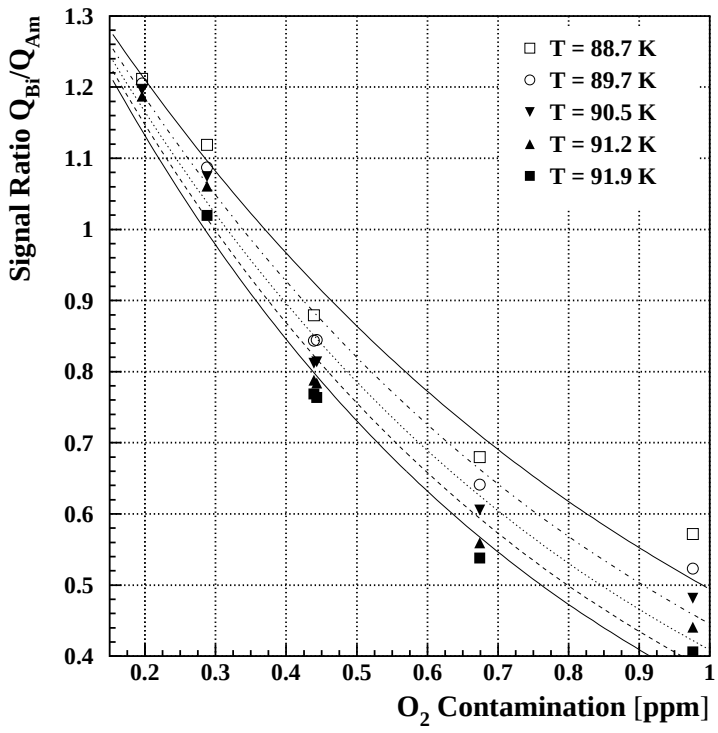

Figure 17. Calibration of the signal ratio of the measured charge in the two cells of the purity monitors for different liquid argon temperatures. The curves are the results of fits of the model described in [13] to the data.

ical damage to the detector. During the operation (87 K to 89 K) a knowledge of the temperature is needed to correct the signals coming out of the detector. After studying the possible options for temperature probes for liquid argon, platinum PT-100 resistors were selected from the possible candidates. They consist of a small ceramic cylinder of 1.6 mm diameter and 12 mm length. This is a standard product of "ABB Automation Products GmBh" (Germany), model W60/69, which, without any further modifications, provides a precision for temperature measurements of the order of 100 mK. The probe resistance is about 100 Ω at room temperature and drops to about 25 Ω at liquid argon temperatures. All probes were read out using a 4-wire connection circuit utilizing a 1 mA measuring current.

To meet the requirement to measure the temperature of the liquid argon with a precision better than 10 mK, all probes were passed through an exhaustive calibration procedure. During the first step, the probes were subjected to a thermo-cycling treatment: 50 cycles of cooling down to liquid nitrogen temperature and warming up to room temperature. This stabilizes the probes deformation and subsequently permits consistent temperature measurement accuracy. As a second step, groups of 16 probes were placed in a thermal bath with a reference thermometer. The probes were calibrated at typically 14 temperature points from 300 K down to 75 K, with most points concentrated around 88 K, and the absolute temperature was measured by the certified thermometer with a preci-

2007 JINST 2 P05005

sion of about 1 mK. The measured points were fitted with a 6th order polynomial (T=f(R)), which allows the calculation of the temperature for a given resistance of the probe. Each probe provided to ATLAS was accompanied by the set of such coefficients.

Special copper blocks were designed to mechanically fix the probes on the HEC modules. Each block, housing one probe, minimized the heat flow via the connection cables to the probe and was mounted on the module rear surface with a good thermal contact. A total of 192 copper blocks with probes were mounted on the rear surfaces of all 4 HEC calorimeter wheels. The 48 copper blocks at the rear surface of a wheel were arranged in 3 arcs — Inner (Radius = 705 mm), Middle (Radius = 1105 mm) and Outer (Radius = 1985 mm). Every second module of a given wheel holds 3 probes. The probes of a rear wheel are shifted by $\pi/32$ in the ϕ-direction compared to a front wheel. The cables from the probes located at each radius were routed to a single feedthrough of the cryostat.

4. Wheel testing and end-cap installation

After closing an end-cap cryostat, the end-cap was cooled down and the final cold QC tests prior to the movement to the ATLAS pit were performed. The cool down and warm up period took about two months. The QC tests in the cold took about six weeks. The QC tests included time-domain reflectometry measurements and cabling checks of all signal and calibration lines, full calibration and delay scans of all signal channels, full pulse-shape analysis of all signal channels, detailed noise measurements [14] of all channels, including coherent noise, and a long term HV test of all HV lines. Typically 3 signal channels per end-cap were found non-operational, corresponding to a 0.1% failure rate. The level of shorted HV lines in the cold was about 2.5%, but after removing the liquid argon from the cryostats the number went down to $\sim 0.6\%$. Most importantly, with four individual HV lines per HEC gap, all HEC regions were active. Thus an excellent missing energy measurement in the full HEC acceptance is assured. Finally, both end-caps have been moved to the ATLAS pit, and the final integration into the ATLAS detector has started (see figure 18).

5. Beam tests

5.1 Beam tests of HEC modules

About 25% of the series production modules were exposed to beams of electrons, pions and muons with energies up to 200 GeV [10]. Two "partial HEC wheels" (three HEC front and three HEC rear modules) were used in a standard setup. The goal was not only to prove the uniformity of the production modules as defined by the hardware tolerances, but also to study the performance and calibration as obtained from pions, electrons and muons. The analysis of the data [10] taken with electrons gives an energy resolution:

$$\frac{\sigma(E)}{E} = \frac{a}{\sqrt{E\,[\mathrm{GeV}]}} \oplus b \tag{5.1}$$

with a sampling constant $a = (21.4 \pm 0.1)\%\sqrt{\mathrm{GeV}}$ and a constant term b compatible with zero, in very good agreement with Monte Carlo (MC) simulations. Horizontal and vertical scans with

2007 JINST 2 P05005

Figure 18. One of the two end-cap cryostats being lowered into the ATLAS experimental cavern. The entrance to the LHC tunnel can be seen on the left, partly hidden by the cryostat.

beams across the surface of the calorimeter showed a homogeneity of the electron signal of $\pm 1\%$ without corrections. The irradiation with pions is of particular importance for the prediction of the final performance of the calorimeter for jets. Using the parameterization mentioned above, a sampling constant of $(70.6 \pm 1.5)\%\sqrt{\text{GeV}}$ and a constant term of $(5.8 \pm 0.2)\%$ were obtained. The data have been compared in detail to MC simulations and the results are published in [15].

5.2 Calibration with beam tests

In 2002 a new phase of combined beam tests was started: the calibration of full ϕ wedges of the three ATLAS liquid argon end-cap calorimeters as specified already in [3]. The main issue is to define calibration procedures and constants for ATLAS.

The first combined beam test carried out in 2002 was devoted to the region $1.6 < |\eta| < 1.8$ [11, 16, 17]. Figure 19 shows the setup of an EMEC module, three front HEC and two rear HEC

2007 JINST 2 P05005

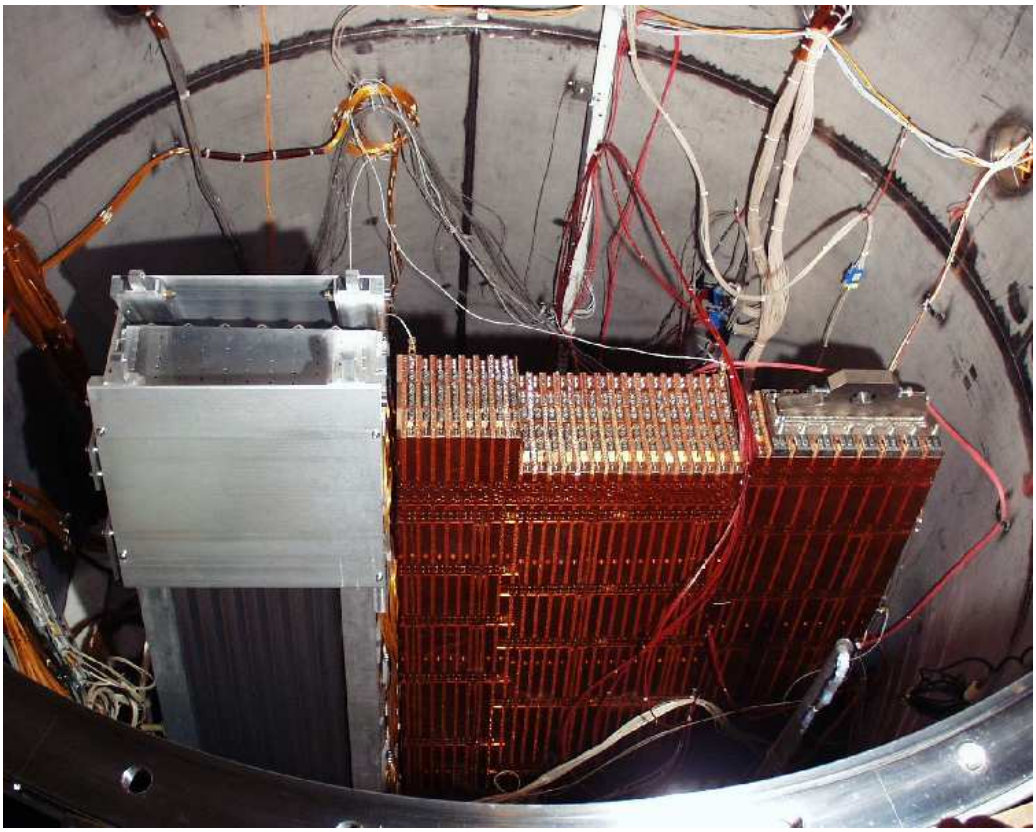

Figure 19. Top view of the first combined beam test showing in the cryostat (from left to right) the EMEC module with the pre-sampler, the three HEC front modules and the two HEC rear modules of reduced longitudinal size.

modules in the cryostat.

First steps of the ATLAS hadronic calibration strategy [18] have been tested. A 3D clustering algorithm and signal weighting approach, as used already in previous experiments, have been tested and the first results yield a very good pion resolution. Figure 20 shows the energy dependence of the energy resolution as compared to various MC predictions.

Fits to the data with formula (5.1) yields sampling constants of $(84.6 \pm 0.3)\%\sqrt{\text{GeV}}$ and $(81.7 \pm 0.4)\%\sqrt{\text{GeV}}$ for π^- and π^+ respectively, and constant terms of zero within errors. The vanishing of the constant terms (after correcting for leakage) shows the effectiveness of the energy weighting approach in achieving a good compensation. The GEANT 3 simulations predict a sampling constant of $(73.3 \pm 0.5)\%\sqrt{\text{GeV}}$ and a vanishing constant term within errors. The GEANT 4 simulations with different hadronic physics lists (LHEP and QGSP) predict sampling constants of $(74.0 \pm 0.5)\%\sqrt{\text{GeV}}$ and $(72.3 \pm 0.9)\%\sqrt{\text{GeV}}$, respectively. In general, the GEANT 4 options are closer to the data, but neither LHEP nor QGSP yield an optimal description. The different energy dependences of the GEANT 4 models are also reflected in a significant constant term: $(4.1 \pm 0.1)\%$ for LHEP and $(2.5 \pm 0.3)\%$ for QGSP. In conclusion, further development and tuning of the hadronic MC simulation are needed.

For ATLAS, the hadronic calibration has to deal with jets rather than single particles; therefore,

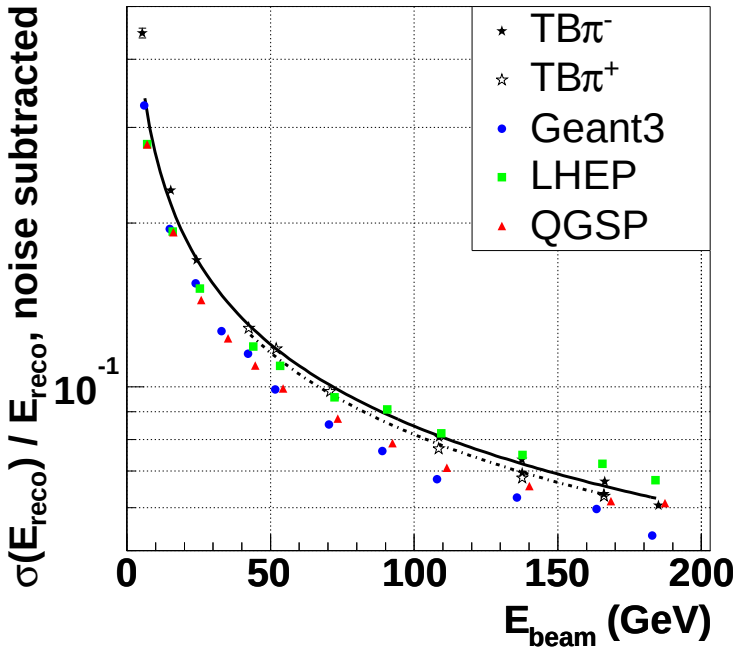

Figure 20. Energy dependence of the energy resolution for π^- and π^+ data taken during the first combined beam test in comparison to different MC predictions. The analysis employs the cluster weighting approach. The lines represent the result of the related fits.

the transfer of weighting constants from beam tests to ATLAS is possible only when using MC simulation. One of the important steps in this procedure is to validate the MC via comparison of the simulation results with test beam data (for details see [15]). Applying this to the energy resolution for jets in ATLAS, it may be concluded that the required sampling term of $50\%\sqrt{\text{GeV}}$ and constant term of 3% will be achieved [4].

The second combined beam test was carried out in 2004 in the region around $|\eta| = 3.2$, the complex region of overlap of the three end-cap calorimeters. The EMEC, HEC and FCAL modules were positioned as in ATLAS, including all details of cryostat walls and supports (dead material). Figure 21 shows the schematic of the setup in the cryostat. One quarter of the full HEC1 and HEC2 wheels were assembled, but with small modules having reduced $|\eta|$ coverage and encompassing only the forward region. Similarly, one EMEC inner wheel module (1/8 of the full EMEC wheel) and 1/4 of the full FCAL1 and FCAL2 detectors were assembled. The data are still being analyzed.

6. Discussion of the as-built variations

The study of the detector construction quality control [12] data shows that the as-built detector has the following limitations:

1. For the energy resolution: the variation in such things as the copper plate thickness, the liquid argon gap and the quantity of liquid argon displaced by the honeycomb mats that maintain

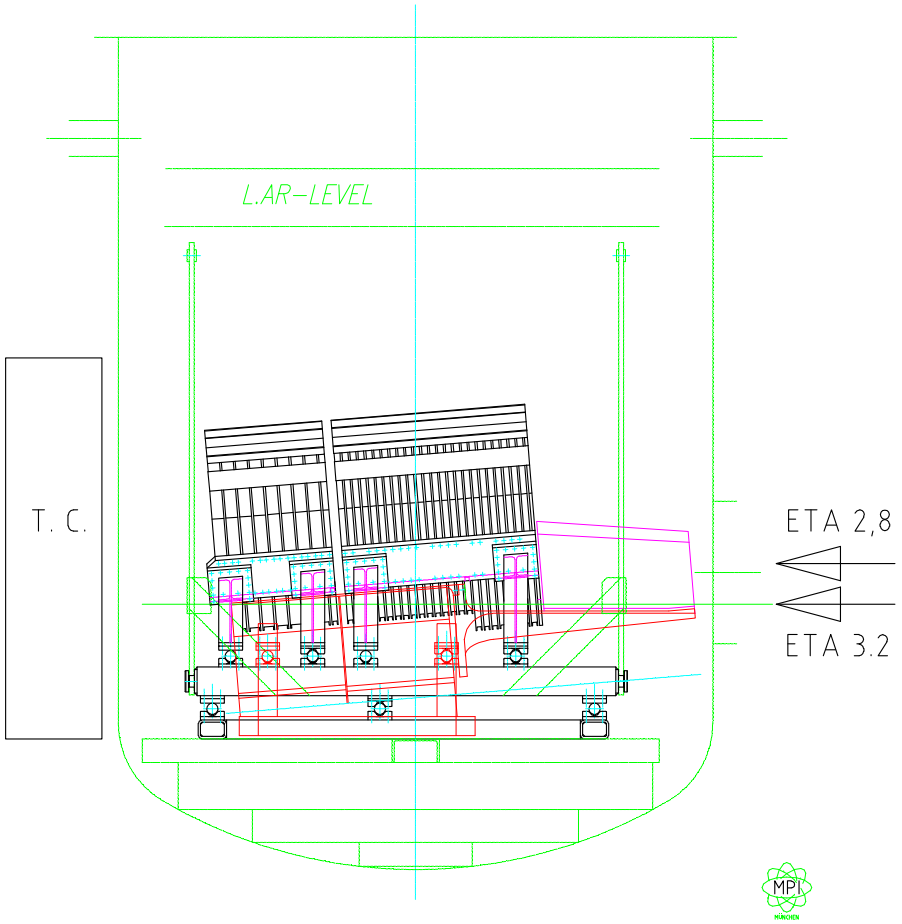

Figure 21. Setup of the second calibration beam run for the region $|\eta| = 3.2$. Here the EMEC, HEC and FCAL modules are positioned as in ATLAS, including all details of cryostat walls and supports (dead material).

the gap, is such that they contribute to the energy resolution at the 0.3% level. Figure 22 shows the distribution of the measured copper plate and honeycomb mat thickness.

2. For the alignment: the tolerance on the alignment between read-out towers is at the level of 1 mm.

3. At the highest LHC design intensities the signal drop due to voltage drops in the high voltage system (including the CLK that distributes the HV in the gaps) will be 0.15% for the first read-out depth and negligible for other read-out depths. The variation in this signal drop will be about 0.06%.

4. Crosstalk between adjacent towers in a module is about 1.5% with an absolute variation of about 0.8%.

5. The positive argon ion build-up in the argon gaps is difficult to estimate due to the lack of knowledge of the argon ion mobility. However, conservative estimates indicate that the

2007 JINST 2 P05005

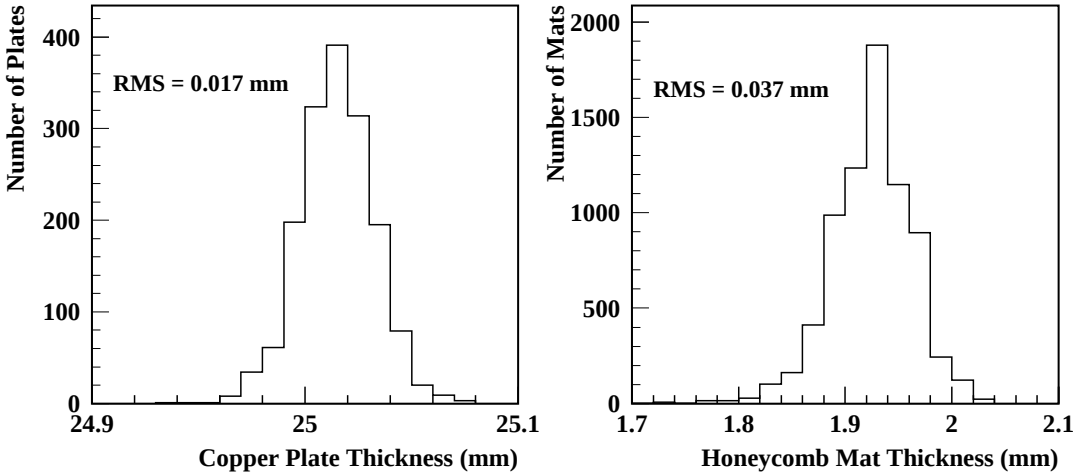

Figure 22. Distributions of measured 25 mm copper plate thickness (left) and honeycomb mat thickness (right).

calorimeter will not have reached critical ion density (when the charge in the ion build up is equal to the charge on the plates) at the highest LHC design luminosities.

These limitations should not seriously effect the operation of the detector at LHC design intensities.

7. Conclusions

The ATLAS hadronic end-cap calorimeter has been successfully constructed, tested, and installed in the ATLAS detector. Test beam measurements of the calorimeter response to single charged pions, together with the use of 3D clustering algorithms and the signal weighting approach to reconstruction, indicate that the resolution for jets will be $\sigma(E)/E = 50\%/\sqrt{E} \oplus 3\%$ (E in GeV) or better, as specified in the ATLAS Technical Design Report [4]. However, not until ATLAS and the LHC are operational will we be able to check if these schemes work successfully in the ATLAS hadronic jet environment.

Acknowledgments

The support of the CERN staff operating the SPS and the H6 beam line, in particular the continuous help of K. Elsener, is gratefully acknowledged. We thank D. Sauvage and the ATLAS liquid argon cryogenics operations team for their invaluable help.

This work has been supported by the Bundesministerium für Bildung, Wissenschaft, Forschung und Technologie, Germany, under contract numbers 05 HA 8EX1 6, 05 HA 8UMA 8 and 05 HA 8PXA 2, by the Natural Science and Engineering Research Council of Canada, by

2007 JINST 2 P05005

the Slovak funding agency VEGA under contract number 2/5137/25 and by the NSF of China under contract number 0051140291. TRIUMF receives federal funding via a contribution agreement through the National Research Council of Canada. We thank all funding agencies for financial support.

References

[1] ATLAS collaboration, *ATLAS Technical Proposal for a general-purpose pp experiment at the Large Hadron Collider at CERN*, CERN-LHCC-94-43, LHCC/P2, 15 December 1994.

[2] G. Macé, S. Prat and J.-J. Veillet, *ATLAS endcap liquid argon calorimeters. Description and construction of the cryostats*, LAL/RT 06-04, May 2006.

[3] ATLAS collaboration, *ATLAS liquid argon calorimeter Technical Design Report*, CERN-LHCC-96-41, ATLAS TDR 2, 15 December 1996.

[4] ATLAS collaboration, *ATLAS calorimeter performance Technical Design Report*, CERN-LHCC-96-40, ATLAS TDR 1, 15 December 1996.

[5] For example see PARTICLE DATA GROUP, *Review of Particle Properties*, *J. Phys.* **G 33** (2006) 287.

[6] R. Wigmans, *Calorimetry energy measurement in Particle Physics*, Clarendon Press, Oxford (2000).

[7] J. Ban et al., *Cold electronics for the liquid argon hadronic end-cap calorimeter of ATLAS*, *Nucl. Instrum. Meth.* **A 556** (2006) 158.

[8] D. Axen et al., *Signal feedthroughs for the ATLAS barrel and endcap calorimeters*, *Rev. Sci. Instrum.* **76** (2005) 063306.

[9] J. Colas et al., *The electrostatic transformer*, *Nucl. Instrum. Meth.* **A 294** (1990) 583.

[10] B. Dowler et al., *Performance of the ATLAS hadronic end-cap calorimeter in beam tests*, *Nucl. Instrum. Meth.* **A 482** (2002) 94.

[11] C. Cojocaru et al., *Hadronic calibration of the ATLAS liquid argon end-cap calorimeter in the pseudorapidity region* $1.6 < |\eta| < 1.8$ *in beam tests*, *Nucl. Instrum. Meth.* **A 531** (2004) 481.

[12] C.J. Oram, *The as-built parameters of the hadronic end cap*, ATL-LARG-PUB-2007-001.

[13] M. Adams et al., *A purity monitoring system for liquid argon calorimeters*, *Nucl. Instrum. Meth.* **A 545** (2005) 613.

[14] E. Rauter, *Studies on noise behaviour and radiation hardness of the ATLAS hadronic end cap calorimeter electronics and power supplies*, Diploma Thesis, Technical University Munich (2005).

[15] A.E. Kiryunin et al., *GEANT4 physics evaluation with testbeam data of the ATLAS hadronic end-cap calorimeter*, *Nucl. Instrum. Meth.* **A 560** (2006) 278.

[16] H. Bartko, *Performance of the combined ATLAS liquid argon end-cap calorimeter in beam tests at the CERN SPS*, Diploma Thesis, Technical University Munich (2003).

[17] ATLAS LIQUID ARGON EMEC/HEC collaboration, *Muon results from the EMEC/HEC combined run corresponding to the ATLAS pseudorapidity region* $1.6 < |\eta| < 1.8$, ATL-LARG-2004-006 (2004).

[18] C. Alexa et al., *Hadronic calibration of the ATLAS calorimeter*, (2003); http://atlas.web.cern.ch/Atlas/GROUPS/LIQARGSOFF/CalibnAlignmnt/index.html.

2007 JINST 2 P05005